ANNALS OF GEOPHYSICS, 69, 1, DM104, 2026; doi:10.4401/ag-9506
OPEN ACCESS

Insights into the Salse di Regnano mud volcanoes: integrating geomagnetism, UAV photogrammetry and historical data

Arianna Pesci[*,1], Roberto Carluccio[2], Francesca D'Ajello Caracciolo[3], Iacopo Nicolosi[4]

(1) Istituto Nazionale di Geofisica e Vulcanologia, Sezione Bologna, Bologna, Italy
(2) Istituto Nazionale di Geofisica e Vulcanologia, Sezione Roma 2, Roma, Italy

Article history: received November 28, 2025; accepted January, 2026

Abstract

This study investigates the Salse di Regnano mud volcanoes within the framework of an INGV project by integrating geomorphological, geochemical, historical and remote-sensing data. Morphological and geochemical analyses reveal distinctive geometric features and enable reconstruction of the historical configuration of the area. Drone-based geomagnetic surveys combined with digitized historical maps transformed into normalized 3D models, together with high-resolution topography derived from Structure-from-Motion photogrammetry and satellite imagery, allow a comprehensive analysis of surface and subsurface patterns. The resulting geomagnetic anomaly maps display a tongue-shaped zone of low values descending from the northern upper slope into the main mud area and broadly aligning with relative morphological features, while additional anomalies highlight structures of potential geophysical interest. Historical evidence indicates a markedly different summit in the early 20th century, dominated by a prominent emission cone that reshaped the area following a paroxysmal event in the 1930s. These results demonstrate the value of integrating modern geophysical measurements with historical and morphological information to advance the understanding of mud volcano evolution.

Keywords: Mud Volcanoes; UAV; Geomagnetism; Historical Data

1. Introduction

The Salse di Regnano, located in the Modena Apennines, are among the most prominent active mud volcanoes in Emilia-Romagna. They form from the upward migration of clay-rich fluids and gases through tectonic fractures and are closely linked to regional geodynamics, driven by compression between the African and European plates and the accumulation of organic material in pre-Quaternary formations, which can generate methane and mud under specific pressure-temperature conditions. Similar patterns have been documented in other Italian mud volcanoes, where fluid migration and surface morphology are strongly influenced by local lithology and tectonic structures (Accaino et al., 2007; Bonini et al., 2007; Bonini, 2009; Mazzini and Etiope, 2017; Brighenti et al., 2020;).

The geological setting is characterized by alternating clayey and marly formations of the Epiligurian succession, interspersed with landslide deposits and Quaternary colluvial cover. These units play a key role in controlling both the location and persistence of mud vents, as fine-grained lithologies favor fluid ascent and the development of overpressure zones.

Figure 1 shows the geological map of the study area, derived from the Carta Geologica d'Italia and regional sources (De Nardo et al., 2019), illustrating the main lithological units and the present day active areas surrounding slope deposits.

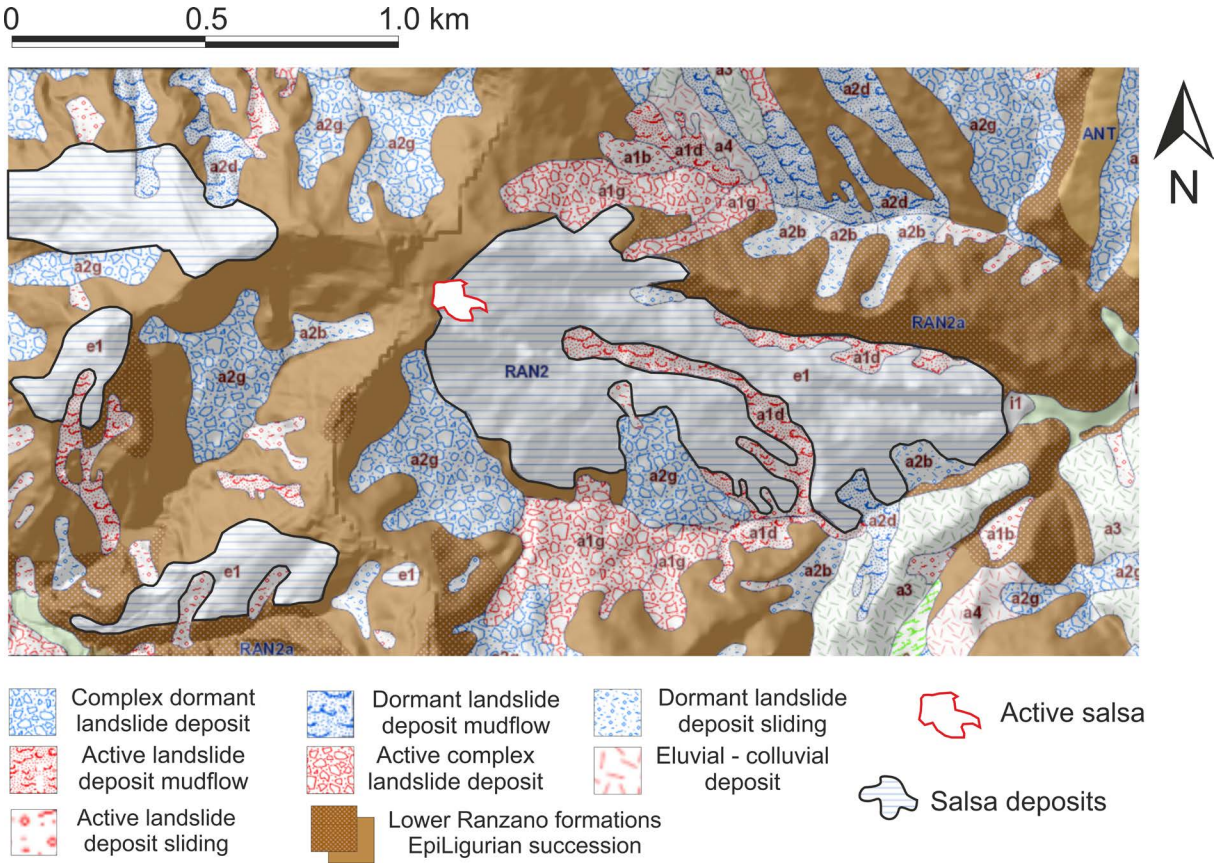

Figure 1. Geological map of the Salse di Regnano area. Main lithological units: clay and marl formations of the Epiligurian succession, Quaternary landslide and colluvial deposits. The present-day area of the Salse di Regnano is indicated by red lines.

Despite their striking appearance, mud volcano systems are complex to interpret and benefit from a multidisciplinary perspective that integrates geophysical and chemical surveys, traditional field measurements, remote sensing, and historical cartographic sources (Nespoli et al., 2023; Bonaposta et al., 2018; Oppo, 2009). Combining these diverse datasets allows reconstruction of the long-term evolution of the systems, the distribution of fractures and deposits, and modifications induced by natural processes or human activities. Such an integrated perspective is also essential for monitoring, conservation, and territorial planning in areas where mud volcanoes coexist with settlements and infrastructure.

A recent study by Pesci et al. (2025a) presented a multidisciplinary investigation of the Salse di Regnano, combining historical records with high-resolution morphological models derived from photogrammetric flights and Structure-from-Motion (SfM) analyses, a method validated as reliable for geoscience applications (James and Robson, 2012; Westboy et al., 2012) and directly compared with terrestrial laser scanning (Teza et al., 2016). Their findings highlighted that current activity is relatively modest, yet significant morphological differences were observed compared to the past, as first reported by Biasutti (1907). Variations of several meters suggest a paroxysmal event in the early 20th century, likely around the 1930s, also documented in contemporary newspapers. One of the most notable eruptions occurred in 1930, when mud was ejected up to ~10 m, the main cone rose by 4 m, and rumbling

sounds were heard kilometers away, as reported by Luigi de Buoi. Other significant eruptions were recorded in 1754, 1796, and 1881 (https://ceastresinarosecchia.it).

This paper expands on these results by presenting a drone-based geomagnetic survey aimed at constraining subsurface features, alongside a 3D reconstruction of the historical topography from the early 20th century, integrated with normalized models to provide an intuitive visual assessment of morphological and magnetic patterns.

2. Geomagnetic Survey

The geomagnetic survey measures local variations in the Earth's magnetic field, a global-scale phenomenon modulated at smaller scales by the composition and structure of rocks. Ferromagnetic minerals can produce anomalies that slightly alter field intensity; when accurately mapped, these variations provide insights into the distribution and characteristics of subsurface materials. Recent advances in drone-borne magnetometry have enabled systematic, high-resolution acquisition of such signals, supporting a wide range of applications from geological and mineral exploration (Malehmir et al., 2017; Parvar et al., 2017; Cunningham et al., 2018; Romero-Toribio et al., 2025) to environmental monitoring and infrastructure assessment (Stoll and Moritz, 2013; Mu et al., 2020; Accomando et al., 2022). Flying tens of meters above the ground, UAV-mounted sensors record dense data grids, producing detailed magnetic anomaly maps and allowing rapid, non-invasive characterization of spatial variations across the study area. These maps often reveal sharp contrasts, interpretable as lithological differences, alongside more regular patterns that may indicate buried structures or conduits, as well as localized anomalies corresponding to discrete bodies. When combined with geological, morphological, and normalized 3D models, such observations enhance understanding of both surface and subsurface dynamics.

Geomagnetic interpretation, however, requires particular caution. Measurements are sensitive to multiple external factors, including anthropogenic metallic objects, diurnal variations of the geomagnetic field, flight altitude, instrument sensitivity and calibration, and ionospheric or solar disturbances. Discriminating geological signals from spurious noise is therefore essential, and interpretations are more reliable when supported by independent datasets.

Today, geomagnetic surveying is applied in various scientific fields. In archaeology, it enables detection of buried structures, such as walls, ditches, or tombs, without excavation (Boschi, 2012; Leucci et al., 2015; Cella and Fedi, 2015). In geophysics, engineering, and environmental monitoring, it supports mapping of igneous intrusions, faults, mineral bodies, and underground infrastructure (Nicolosi et al., 2019; Nikulin and de Smet, 2019; Hammack et al., 2020; Accomando et al., 2025).

Integrating drone-based geomagnetics with topographic, photogrammetric, and multispectral models provides a modern, non-invasive, and effective approach for investigating both natural systems and anthropogenic contexts.

In drone-based geomagnetic surveys, the magnetometer is the key component, designed to detect small variations in the Earth's magnetic field with high precision. Modern aerial magnetometers are lightweight and compact, often integrating auxiliary sensors such as gyroscopes, accelerometers, and GPS, which record the instrument's orientation and position during flight. These data allow corrections for displacements, vibrations, and rotations that could otherwise compromise measurement accuracy (www.sphengineering.com).

To reduce magnetic interference from the UAV, the sensor is suspended several meters below the aircraft using a lightweight cable, minimizing disturbances from motors and metallic components while ensuring a stable trajectory (Pisciotta et al., 2021). The overall weight of the system is critical, as every additional gram affects the drone's stability and autonomy; UAV magnetometers are typically engineered to weigh only a few kilograms, including their battery (www.gemsys.ca). This setup enables rapid and flexible deployment. The drone follows predefined flight grids while the suspended magnetometer continuously records magnetic field variations. Collected measurements are subsequently processed to generate high-resolution subsurface maps, combining the accuracy of geomagnetic sensing with the mobility and efficiency of UAV platforms. Integration with normalized 3D models allows immediate visual assessment of spatial patterns and facilitates comparison with topography and historical reconstructions.

Here, the geomagnetic survey was conducted using an aeromagnetic measurement platform designed and built by our research group. The platform, referred to as the "Bird," houses all sensors and electronics in an aerodynamic case. Its core element is an optically pumped rubidium vapor magnetometer developed by QSpin (https://quspin.com), providing a miniaturized total-field magnetometer tailored for aeromagnetic prospecting. The QTFM (QuSpin Total-Field Magnetometer), including electronics, weighs less than 100 g, with compact dimensions and low power consumption, making it particularly suitable for UAV applications. The main characteristics are listed in Table 1.

Table 1. Magnetometric system sensors and parameters.

Parameter	Value	Note
Sensitivity	<3 pT/√Hz	Scalar
Data Rate	up to 1000 samples/s	–
Deadzone	<±7°	Axial only
Heading Error	<3 nT	Uncompensated
Dynamic Range	1000 – 150,000 nT	–
Sensor Head Size	17.7 × 19.8 × 35.8 mm	–
Electronics Unit Size	14.7 × 24.4 × 92.3 mm	–
Sensor Head Weight	12 g	–
Electronics/ECU Weight	29 g (6.5 g without housing)	–
Voltage Input	5 V (via SCB)/10-12 V (direct)	–
Power Consumption	2.5 W (operating)/3.5 W (startup)	–
Max Gradient Field	300 nT/cm	–

A heading error of approximately 3 nT may be relevant in areas with very low magnetic anomalies, but it can be effectively corrected during data processing using numerical procedures. The aeromagnetic platform integrates the QSpin magnetometer with a datalogger recording information from multiple sources. Positional data are acquired by GPS at 5 Hz, orientation by an Inertial Measurement Unit (IMU), and altitude relative to the take-off point by a barometric altimeter. A laser altimeter with an effective range exceeding 40 m is included to measure vertical distances from natural obstacles such as trees. All parameters are stored in text format on an SD card.

Selected data are transmitted in real time to a ground station via a LoRa (Long Range) transmitter. Despite limited bandwidth, the system sends the measured magnetic field, barometric and laser altimeter readings, geographic coordinates, and a recording-status flag. At the ground station, a receiving unit connected to a PC logs the transmissions, while custom software visualizes each measurement point with spatial coordinates and a color scale proportional to magnetic intensity. A cartographic background allows operators to monitor the flight path relative to local landmarks. Integration with normalized 3D models enables immediate visual comparison of magnetic patterns with topography and historical reconstructions.

All electronics are housed inside an aerodynamic case, 1 m in length, equipped with a tail and stabilizing fins, and suspended 10 m below the UAV by a non-magnetic cable (Fig. 2). This arrangement ensures mechanical independence between the UAV and the aeromagnetic platform, minimizing magnetic interference while maintaining operational flexibility. The UAV follows a constant altitude above the terrain, guided by onboard RTK-GPS and a preloaded flight model for precise positioning. The magnetometer case is equipped with a dedicated GPS, IMU, barometer, LiDAR, LoRa radio link, battery, SD card, and microprocessor, enabling autonomous data acquisition. In the implemented system, both magnetic and GPS measurements are managed by a single onboard logger, which rapidly queries the magnetometer and records the corresponding GPS position almost simultaneously, within a few hundredths of a second. The two datasets are therefore stored together in a single database, providing direct spatial attribution of magnetic measurements without the need for post-processing time-stamp synchronization. Given the low survey

speed, this acquisition strategy ensures accurate positioning of the magnetic data. Flight tests confirmed safe operations at altitudes between 10 and 50 m above ground, with line spacing between 20 and 50 m depending on site logistics.

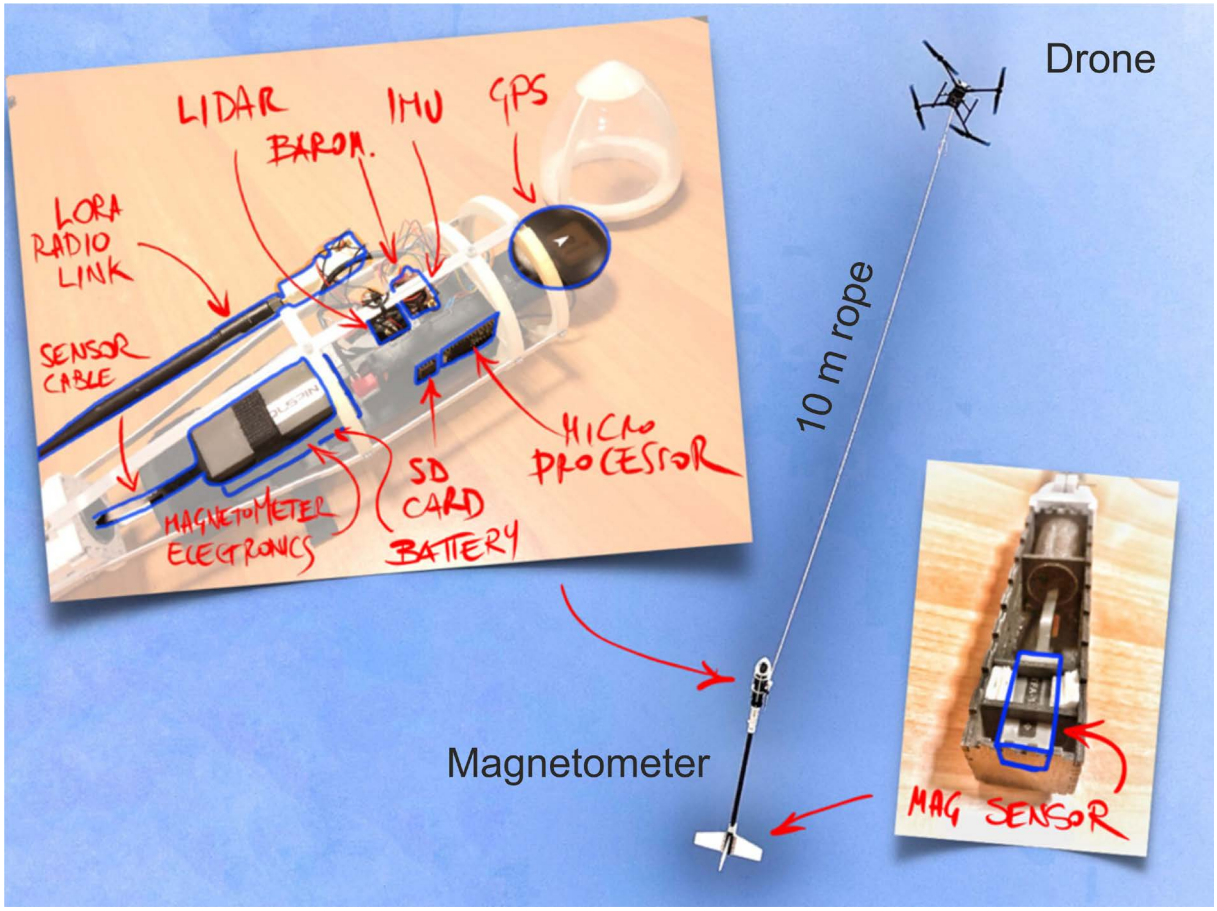

Figure 2. The assembled magnetometric platform, showing all integrated components. In the background, the UAV is visible, carrying the magnetometer suspended beneath it by a 10 m cable over the survey area.

3. Magnetic model and data exploring

For the Salse di Regnano survey, flights were conducted at an altitude of 30 m with 20 m line spacing. Certain areas could not be surveyed due to nearby houses and regulatory restrictions imposed by the Italian Civil Aviation Authority (ENAC), which prohibits flights over buildings, urban areas, or gatherings of people without authorization. The resulting magnetic anomaly map shows values within ± 10 nT.

In theory, anomaly intensity decreases with distance from the source following an inverse-cube law ($1/r^3$), although this is a simplified approximation. At an altitude of approximately 30 m, anomaly intensity may decrease by up to 50%, depending on geological characteristics and subsurface composition. Flying at higher altitudes improves survey efficiency by covering larger areas more quickly and reduces local surface interferences, while the 10 m sensor offset effectively eliminates UAV-induced disturbances. However, higher altitudes also reduce spatial resolution, as the sensor integrates the magnetic field over a larger volume, decreasing sensitivity to subtle subsurface variations.

The anomaly map (Fig. 3) reveals a clear pattern: a tongue of negative anomalies, ranging from 0 to –8 nT, extends in a S-SE direction across the active mud area. Surrounding near-zero values form a subtle boundary, itself encircled by positive anomalies up to +8 nT, resulting in a clear visual contrast. The main emission vent corresponds to the sharp transition from positive to negative anomalies. In the northeastern portion of the surveyed area, a pronounced negative anomaly of –6 nT displays a conical shape resembling mud cones, indicating potential buried structures.

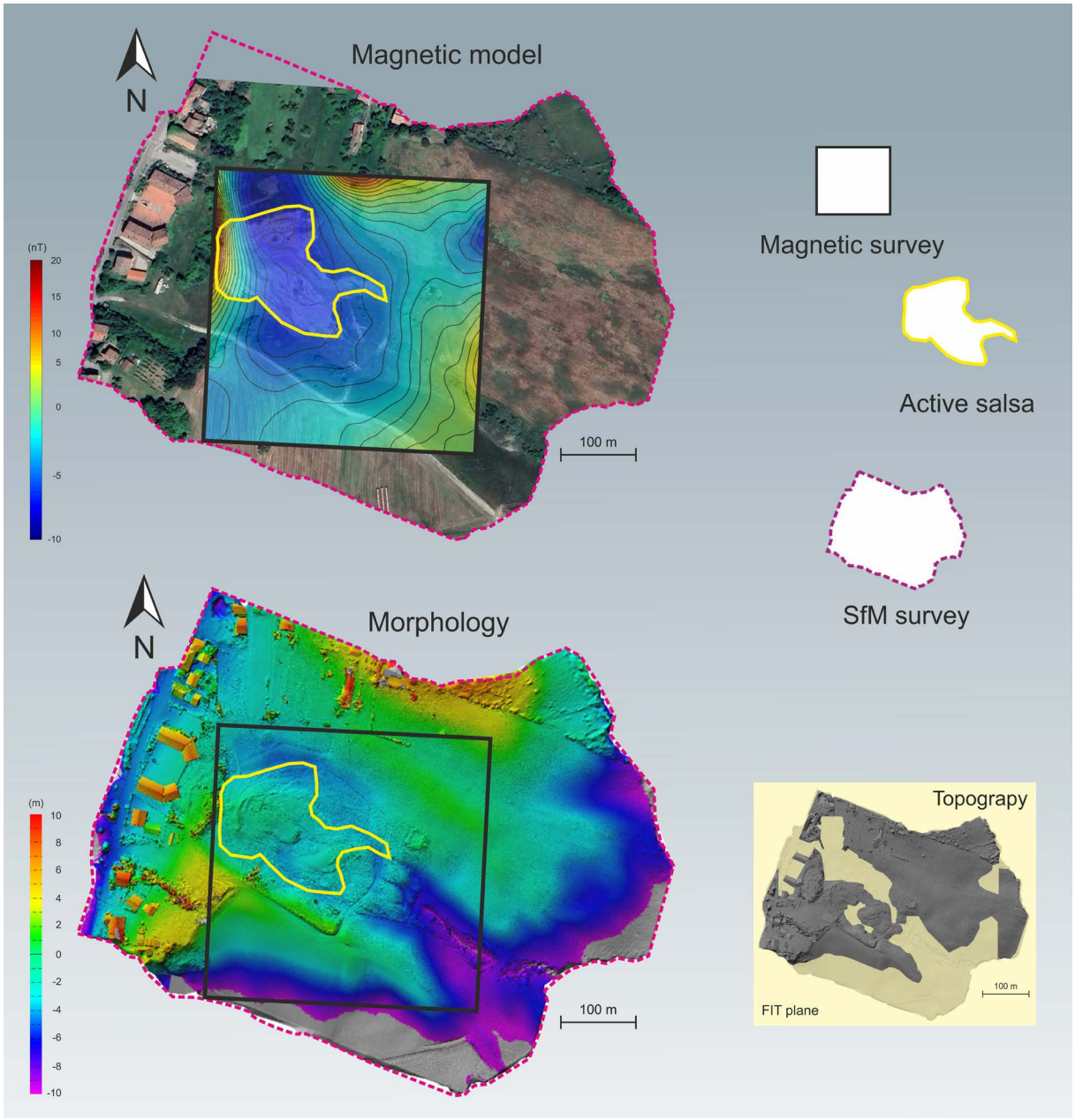

Figure 3. Preliminary geomagnetic map aligned with the topographic model. (a) Morphological model of the area (Pesci et al., 2025a) showing the main zones of interest; (b) Magnetic measurements overlaid on the topographic map of the study area (Google Earth).

Before proceeding, it is essential to perform an initial evaluation of the data and the context in which it was acquired. Assessing reliability, coherence, and stability is crucial to ensure meaningful interpretation. The following section explores the characteristics of the measurements, their spatial distribution, and their correlation with the study area from a morphological perspective.

The magnetometric dataset obtained in this study represents a high-resolution record of near-surface magnetic variations acquired under field conditions. The measurements were collected using a magnetometer suspended approximately 10 m below the UAV by a non-magnetic cable to minimize platform-induced magnetic interference (Accomando et al., 2021; Walter et al., 2021). While slight positional irregularities due to cable oscillation and drone dynamics may occur, these are minor and the resulting data are largely smooth, as confirmed by internal variability analysis (next section). Excessive oscillations were not observed, and no additional low-pass filtering was applied, as the measured values already reflect stable UAV operations (Walter et al., 2019; Accomando and Florio, 2024). Despite careful planning of flight paths, low navigation speed, and continuous monitoring of the sensor's altitude

and position, minor deviations in measurement geometry may still occur. Consequently, a preliminary exploration of the dataset was undertaken to evaluate its characteristics and ensure a proper understanding of the measured signal prior to interpretation. This exploration involved analysing the internal variability of the data, comparing magnetic and topographic information, and investigating potential correspondences between the measured magnetic field and the synthetic anomalies expected from surface morphology. Integration with normalized 3D models further facilitates visual assessment of spatial patterns, highlighting both correspondences and discrepancies between morphology-induced fields and the measured magnetic anomalies. It should be noted that this survey represents a one-off measurement aimed at investigating a small area, with flight durations of only a few minutes. The goal was to highlight spatial differences in magnetic values across the site. Therefore, corrections for hourly or diurnal geomagnetic variations were not applied, as their expected amplitude at the study latitude is of the order of 10-30 nT (e.g., Yamazaki and Maute, 2017).

3.1 Magnetic data variability

A preliminary evaluation of the magnetometric dataset was conducted to assess stability, internal variability, and associated measurement errors across the entire survey. A magnetometric digital elevation model (DEM) was generated by interpolating the measured points onto a regular grid with 1 m spacing, yielding values between –10 and 30 nT. This initial model provided the foundation for subsequent analyses, including the computation of local statistics and the quantification of internal variability, aimed at identifying possible noise components and obtaining a first assessment of overall data quality.

To investigate internal consistency and the spatial distribution of local noise, the grid was subdivided into 5 × 5 m, 10 × 10 m, and 15 × 15 m square blocks. For each block, the minimum, maximum, mean, and range (max-min) were computed, producing four derived maps: local mean, minimum, maximum, and internal variability. The latter directly expresses the magnetic excursion within each block, providing a useful estimate of non-structural fluctuations and residual micro-anomalies (Fig. 4). The mean and extreme value maps reproduce the original magnetic range, whereas the range map exhibits only limited variations, typically between 0 and ≈1 nT, with few localized outliers. This upper value, corresponding to about 3% of the total excursion in the dataset, can be considered a conservative threshold for local measurement and interpolation uncertainty.

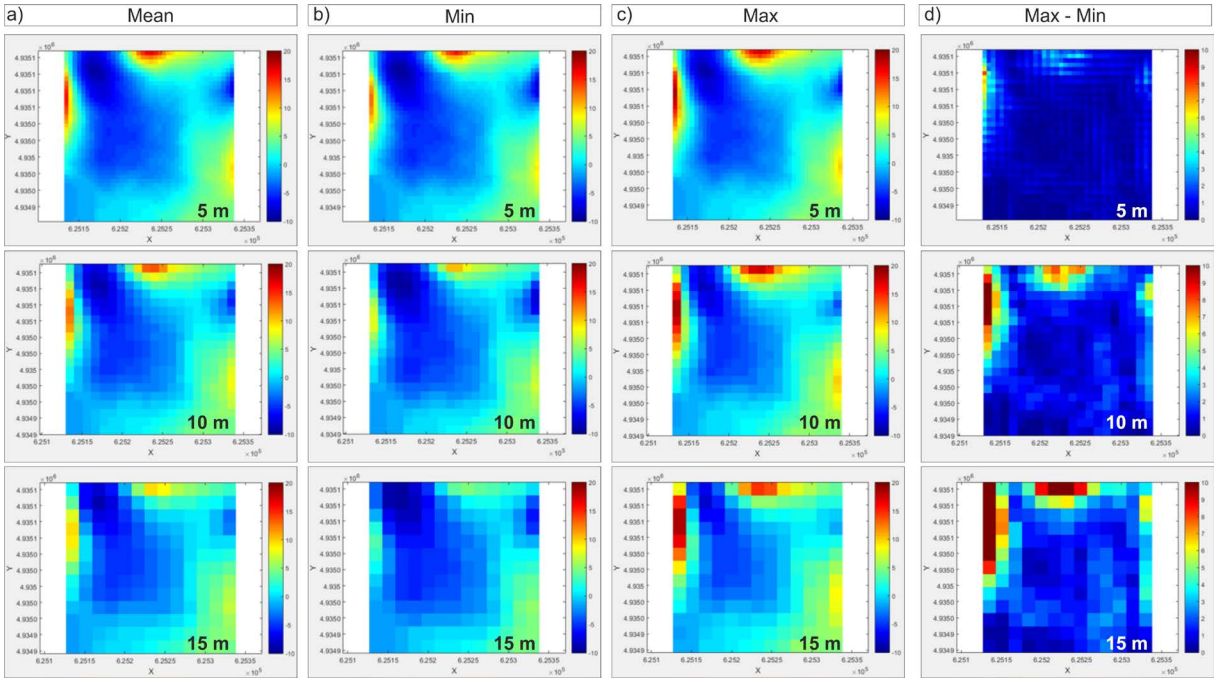

Figure 4. Measurement stability and signal variability represented on a 1 × 1 m grid and variable blocks of 5, 10 m, and 15 m, respectively. (a) Local mean; (b) local minimum; (c) local maximum; (d) range (max-min), providing an estimate of internal variability and potential micro-anomalies.

The spatial pattern of internal variability is largely homogeneous throughout the investigated area, with a slight increase in the upper slope sectors where local gradients are steeper. Such uniformity confirms a good signal-to-noise ratio, suggesting that the detected variations mainly reflect real structural features rather than instrumental or processing artifacts.

This intentionally straightforward approach provides a representative local range of meaningful variability, ensuring a robust basis for further analyses and for quantifying possible deviations linked to survey accuracy or external interference. Integration with normalized 3D representations further facilitates the visual assessment of subtle variations and enhances understanding of spatial patterns in relation to topography and morphology.

3.2 Morphology and magnetism interplay

As an initial step to assess the overall characteristics of the dataset, a visual, side-by-side comparison of the morphological and magnetometric data was performed. The two datasets were carefully co-registered, generating georeferenced point clouds covering the same area. From these, two digital models were derived: DEM_1, representing the deviations of the remotely sensed surface points from a local best-fit plane (capturing the morphological configuration), and DEM_2, containing the interpolated magnetometric values. (Note: in this work, DEM refers generally to any raster-based surface, not only elevation data).

This comparative overview provides a first impression of the spatial organization of the data, allowing the identification of shared or contrasting patterns within a common reference frame. While the magnetic surface shows localized anomalies superimposed on a smooth background, the relative topography exhibits a more gradual relief. Steep slopes or morphological transitions do not systematically correspond to magnetic highs or lows, indicating

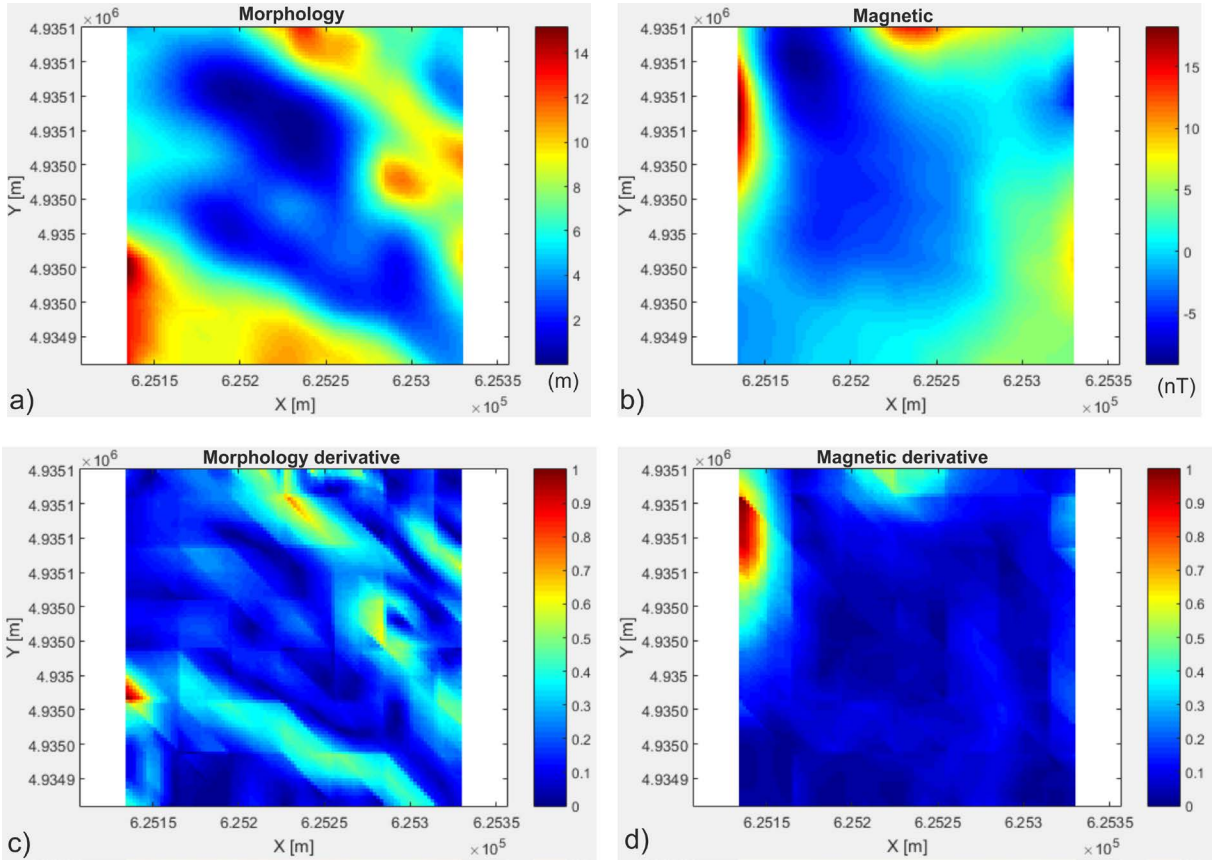

Figure 5. Preliminary visual overview of morphology and magnetometry. (a) Morphology map; (b) Interpolated magnetic field map; (c) Morphological gradient (normalized); (d) Magnetic field gradient (normalized). The top row shows the raw spatial distribution, while the bottom row highlights the rate of change in each dataset, providing an initial observational perspective on their spatial variability.

that the observed magnetic variations are largely independent of surface geometry. Figure 5 presents this overview in a 2×2 matrix: the top row shows the topographic and magnetic maps, while the bottom row displays their respective spatial derivatives, normalized to emphasize rapid changes. This arrangement highlights the differences in spatial texture and the rate of variability between the two datasets, offering a first, observational "big-picture" perspective before further quantitative analyses. Integration with normalized 3D representations further supports intuitive comparison, helping for visual distinction of areas where magnetic anomalies cannot be directly explained by surface morphology.

Note that the data used to generate the DEMs and especially the derivative maps were originally sampled on a 2 × 2 m grid. For visualization purposes, the datasets were interpolated using the natural neighbor method to produce smooth, easily readable figures without altering the underlying measurements.

3.3 Morphology and induced magnetic pattern

To assess whether the observed scalar magnetic anomalies (total-field UAV measurements) could be explained solely by surface morphology, a forward magnetic model was developed using the high-resolution DEM derived from UAV photogrammetry. Each DEM cell (5 m grid spacing) was treated as a rectangular prism uniformly magnetized along the local geomagnetic field (inclination ≈61°, declination ≈2°), following standard potential-field modelling approaches (Blakely, 1995; Ghirotto, 2023). The magnetic contribution of each prism was analytically computed at the UAV sensor altitude, and the total synthetic anomaly was obtained by summing all individual effects.

Synthetic anomalies were calculated for observation heights of 30 m and 40 m above ground, representing typical UAV flight conditions. As the magnetization properties of near-surface materials were unknown, all results were normalized to emphasize spatial patterns rather than absolute amplitudes.

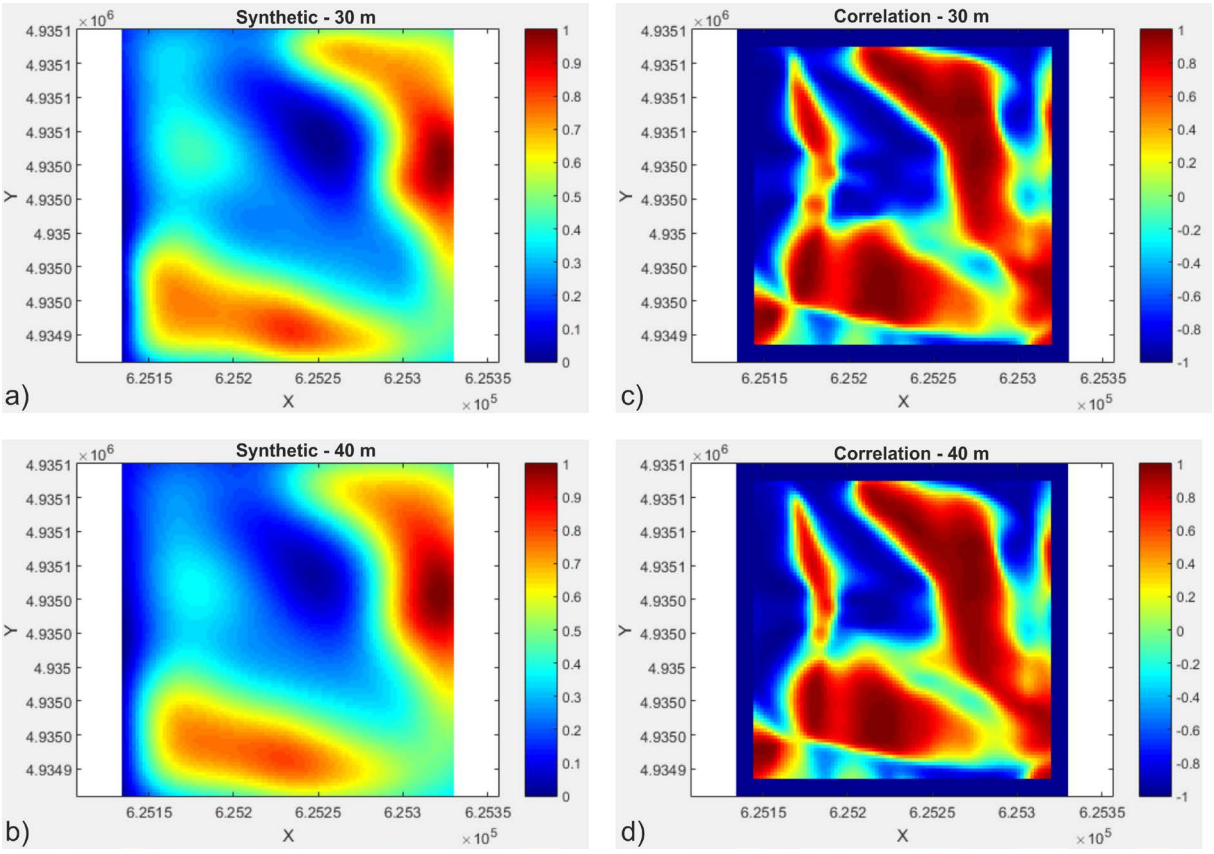

Figure 6. Testing morphology-induced magnetic correlation with measured data. (a) Synthetic field computed with 5 × 5 m cells at 30 m above the terrain; (b) Synthetic field at 40 m above the terrain; (c) Correlation map between measured and synthetic data at 30 m; (d) Correlation map at 40 m above the terrain.

A localized correlation analysis was then applied between the synthetic anomalies and both the measured magnetic field and the surface morphology. Correlations were computed using a moving 5×5-cell window (25 × 25 m terrain segments), allowing a spatially resolved assessment of potential dependencies. The results indicate that, although some sectors show moderate correlation or anticorrelation, large portions of the area remain weakly correlated, particularly across the main negative-anomaly tongue. This confirms that topography-induced magnetic effects alone cannot reproduce the main features of the UAV-measured field.

Figure 6 illustrates the comparison between synthetic anomalies at 30 m and 40 m flight heights and the UAV measurements. While the synthetic fields locally follow terrain gradients, they fail to replicate the overall pattern and polarity of the observed anomalies.

Figure 7 presents a 3D visualization (not to scale) of the normalized datasets, including the morphological model, the measured magnetic field, and the synthetic morphology-induced field. This 3D view provides an immediate, intuitive impression of characteristic spatial patterns, highlighting differences that may not be evident in 2D maps and offering a complementary perspective on the variability of the magnetic signal relative to surface morphology.

The UAV-measured magnetic field exhibits a well defined geometry, with a pronounced area of negative values extending roughly north-south and slightly veering eastward. Synthetic magnetic field computed from the high resolution DEM shows correlations in localized sectors, but their overall spatial distribution differs markedly from the measured field. Comparison of normalized 3D models confirms that topography-induced effects do not generate the same characteristic patterns observed in the UAV data. These observations indicate that the morphology-induced contribution is relatively weak and insufficient to significantly modify the measured magnetic field. 3D visualizations provide an intuitive perspective, making differences between synthetic and measured fields immediately apparent.

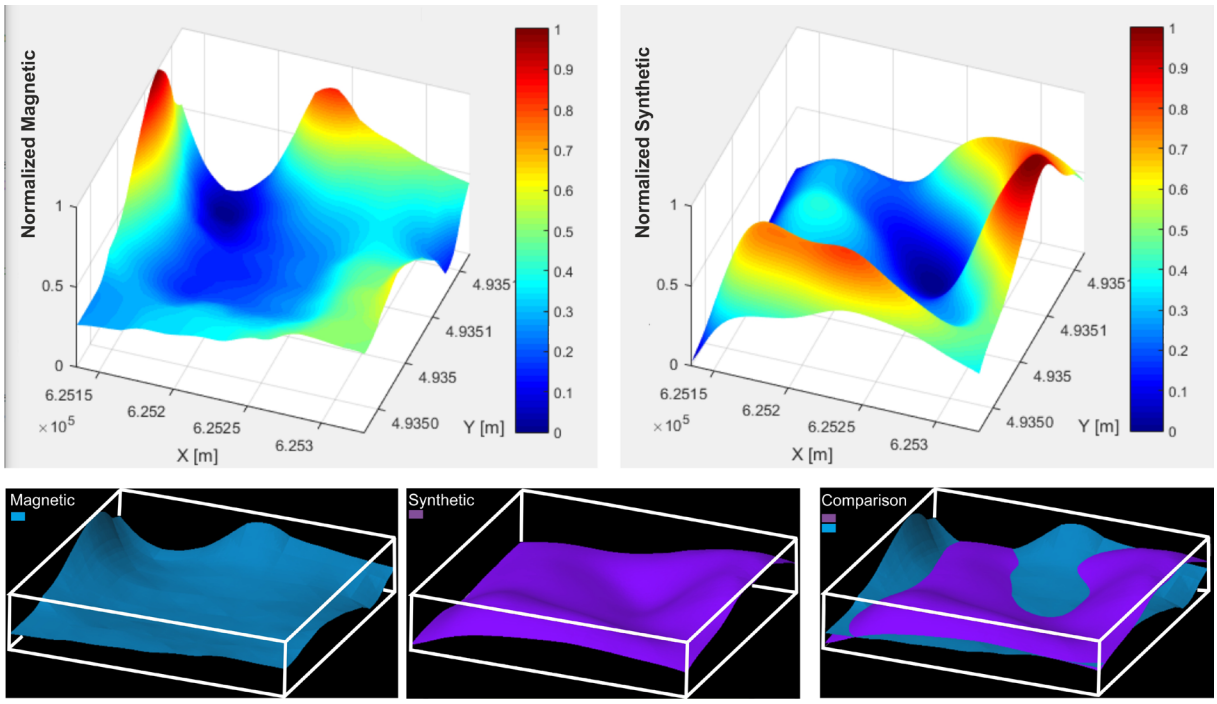

Figure 7. 3D visualization of measured magnetic field and synthetic morphology-induced one. At bottom: a 3D object visualization with colors and overlay.

Figure 8 shows magnetic isolines superimposed on two dataset providing a more detailed comparison of spatial patterns. This arrangement allows direct visual assessment of how morphology-induced effects relate to the measured magnetic field and highlights areas where synthetic and measured patterns diverge or coincide, offering a fine-scale perspective on the morphology-magnetism interplay. As in the previous section, the datasets used for generating synthetic magnetic fields and related visualizations were sampled on a 2 × 2 m grid and interpolated using the natural neighbor method, producing smooth figures for clarity without modifying the original measurements.

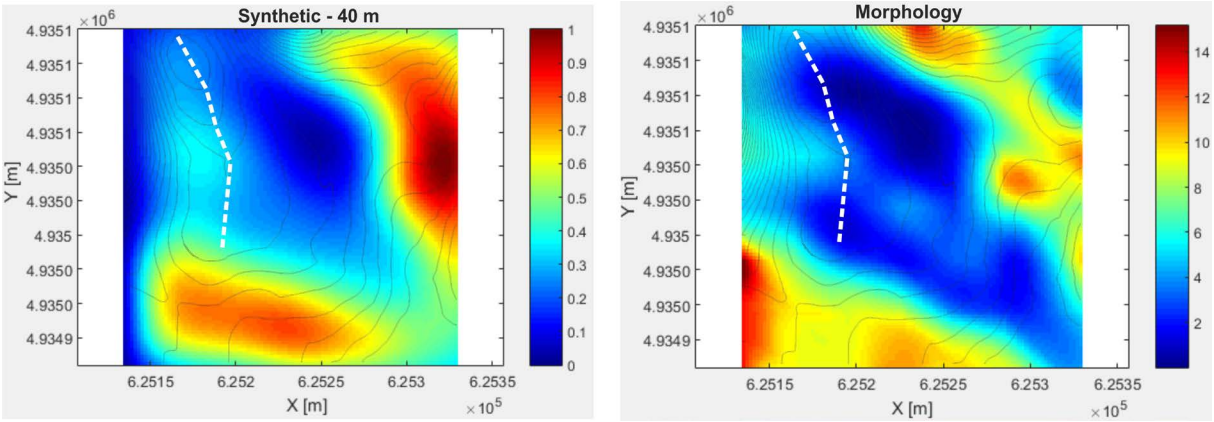

Figure 8. Overall results integrated visualization. (a) Magnetic field isolines over the synthetic morphology induced anomalies; (b) magnetic field isolines over the morphological map. The white dash line shows the main magnetic gradient direction.

3.4 Preliminary evidence from UAV magnetism

From the UAV geomagnetic survey, a detailed map of measured magnetic values was produced and visualized using a false-color scale to highlight spatial variations. The measured magnetic field exhibits a stable and coherent pattern, dominated by a pronounced "tongue" of negative values extending across the main mud-emission area in a roughly north-south direction, slightly veering eastward. Surrounding areas show near-zero values, while positive anomalies cluster along marginal or slightly elevated sectors.

The measured field was compared with a synthetic magnetic model derived from surface morphology, as well as with topographic and morphological-derivative maps. Although correlation maps indicate alternating zones of positive and negative correlation, pointing to localized correspondences between topography and magnetism, these relationships are spatially inconsistent and do not reproduce the overall anomaly geometry. In other words, while areas of correlation and anticorrelation exist, their distribution does not align with the main features of the measured magnetic field.

Normalized maps of the synthetic and measured fields further emphasize that topography-induced effects are weaker and qualitatively different from the observed anomalies. Localized correlations are present, but the synthetic fields fail to capture the dominant structures of the UAV-measured data. 3D visualizations of the normalized datasets provide an intuitive perspective, highlighting the characteristic patterns of each dataset and making the differences between morphology-induced and observed magnetic signals immediately apparent. The geomagnetic anomaly maps also offer a preliminary depiction of the subsurface distribution of materials and potential uprising structures. Positive anomalies may correspond to bodies or sediments with higher magnetic susceptibility, whereas negative lobes indicate genuine decreases in magnetization. At the Salse di Regnano site, negative anomalies generally coincide with active emission zones, while positive anomalies tend to cluster along marginal areas or secondary structures, possibly reflecting more consolidated layers or partially cemented conduits.

Overall, integrating UAV geomagnetic data with relative morphology, normalized models, and 3D visualizations provides tentative insights into the spatial organization of anomalies and the underlying subsurface architecture. These observations suggest that surface morphology contributes only marginally to the measured field, though further analyses are required to fully interpret the origin and evolution of the detected anomalies.

4. Some data from the past

Historical reconstruction of the Salse di Regnano was constrained by the scarcity of early visual documentation. No aerial photographs or detailed maps are available prior to the 1980s, and the few existing historical images are generally of low resolution and limited coverage. Consequently, the reconstruction relied mainly on bibliographic and cartographic sources. Among these, De Nardo (2019) and Biasutti's (1907) map, together with Dainelli's original

article (1907), provided the most valuable information. From these documents, detailed morphological data were extracted, including approximate dimensions of the active area (~140 × 50 m), slope characteristics, cone distribution, and mud accumulation zones.

The planimetric information of the historical model required particular care, as data were limited and supported only by a few descriptive notes in the original report. The first reference is the historical map, where contour lines are clearly shown but no reliable scale is provided: a nominal 1:1200 scale is indicated, but the reproduction does not preserve the original dimensions. The second reference is a topographic profile crossing the area from the summit to the landslide zones and the underlying slope, depicting the same mud zone boundaries as the map. Assuming the profile follows the main topographic gradient, it was used to scale the map and establish a metric planimetric reference. Elevations, however, do not match between the two representations, likely due to different zero-altitude references; therefore, they were not used for dataset alignment. The figure illustrates the method, showing both the original information and its digitized version. The mud volcano area is highlighted, together with measurements of selected map references scaled according to the geometric considerations described above. Several historical photographs are also provided, documenting the main emission cone with associated deposits and different site views.

As reported in the original survey, the planimetric length of the central active mud zone, corresponding to the lighter-colored area where clay accumulates, was estimated at ~131 m, while 202 m represents the total extent of the mud volcano area including surrounding debris and landslide deposits along the slope. A key challenge was the lack of a reliable horizontal scale in the historical maps: although contour lines with elevation values were provided, their relation to actual distances was unclear. To address this, the data were digitized and scaled using tracing techniques in a MATLAB application, which allows the operator to trace contours, assign elevations, and infer a consistent horizontal scale by interpreting spatial relationships among morphological features. This approach

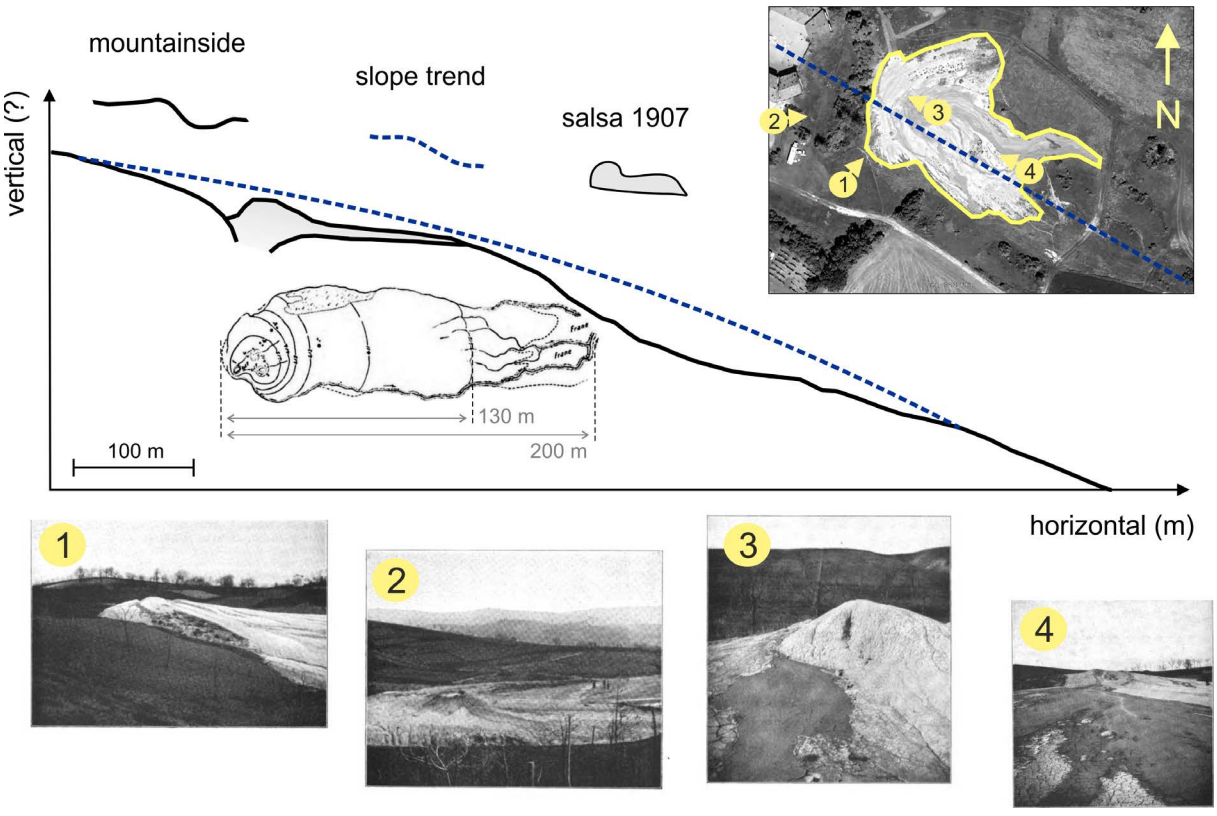

Figure 9. Digitized and redrawn historical profile with the 1907 mud-volcano area highlighted in gray, together with the rough topographic map produced at the time. The top-right inset shows the current mud-volcano area on an aerial view, with the inferred 1907 profile (dashed line) and the presumed historical shooting locations (yellow dots). Arrows indicate the viewing directions. The four historical photographs from 1907 (bottom), numbered accordingly, correspond to these viewpoints.

ensures precise and repeatable handling of large vector datasets, minimizing manual errors and enabling alignment of the historical 3D model with the current topography based on morphological boundaries.

In this section we will provide an example of using sub-sections and also tables.

4.1 Real scale DEM creation

A dedicated MATLAB-based software (DigMap) described in a recent technical report (Pesci and Randazzo, in press) was developed to transform historical cartographic material into metrically consistent datasets suitable for subsequent geomorphological analyses. The software implements a structured workflow consisting of: 1) Image import and scaling: a historical map or sketch is imported as a raster image. The user defines spatial references by selecting two points of known distance, which allows the conversion of image pixels into real-world units; 2) Interactive digitization: topographic features such as contour lines, profiles, or boundaries are traced interactively with the mouse. Each line can be associated with an elevation value or descriptive attribute; 3) Data export: the digitized features are stored as structured datasets with X, Y, Z coordinates, suitable for further processing or integration with other datasets; 4) Interpolation and model generation: the point and line data are interpolated over a regular grid to generate a digital terrain model (DEM) or a point cloud, which can be visualized using false-color maps or 3D plots; 5) Rescaling and alignment: the resulting models can be rescaled or aligned to match different reference systems, enabling direct comparison with modern photogrammetric or remote-sensing data.

Applying this workflow to Biasutti's (1907) map allowed the reconstruction of a historical DEM. Although the model is characterized by low spatial resolution, it provides a valuable reference for comparison with the present-day configuration (Fig. 10). This is an indentation for sub-sections.

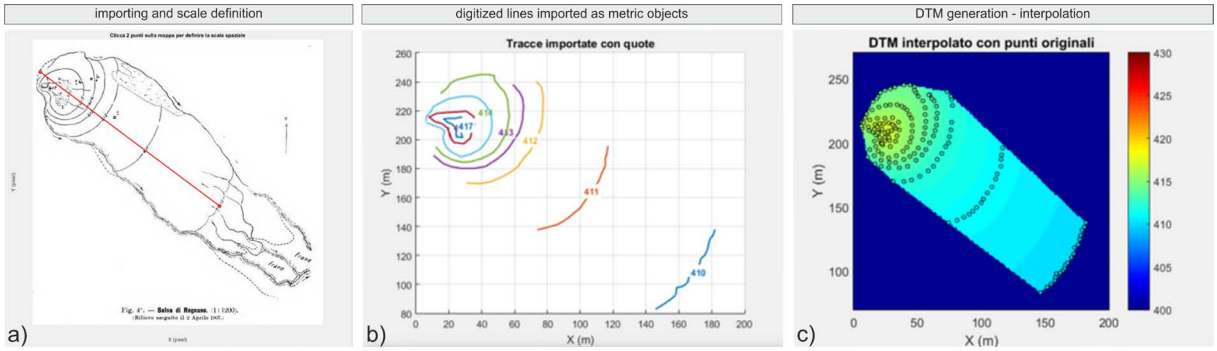

Figure 10. Main interface of the digitization workflow. (a) Definition of a reference distance by selecting two points on the historical map to calculate scale; (b) interactive digitization of contour lines and boundaries; (c) generation of a preliminary DTM from traced data.

4.2 Models comparison

The availability of the 1907 model, albeit at low resolution, enables comparison with the 2025 configuration. Since the two datasets are in different reference systems, the 1907 model was aligned onto the 2025 model using roto-translation operations, without altering its scale. Alignment was performed in Polyworks (Innovmetrics), a flexible environment optimized for data integration. The results, shown in Fig. 10, indicate that the summit area in 1907 featured a truncated cone slightly displaced and higher than today. Difference maps reveal variations of up to ~5 m, highlighting areas of material accumulation or loss and illustrating how past events reshaped deposition zones and the locations of emission vents.

A preliminary volumetric estimate over the area common to both models, obtained via triangulated models oriented with respect to the same arbitrary plane (Pesci et al., 2018), shows a positive residual of ~1450 m^3 across the general area. In contrast, the summit area exhibits a negative residual of roughly –1650 m^3. These relative volumes, consistent with the difference maps, suggest that the summit experienced material loss and transformation of the

cone shape due to destructive events, while within the main mud body, material accumulation and displacement occurred in both positive and negative residual areas.

It is important to note that these volume calculations are relative, derived from two aligned models; therefore, deviations from the absolute historical configuration may exist. Nevertheless, the qualitative insights regarding material redistribution and summit transformation remain valid. The chosen color scale highlights differences between the 1907 and 2025 morphologies (Fig. 11).

It should be noted that, despite careful alignment using roto-translation operations, the historical 1907 map inherently carries uncertainties due to limited scale information, sparse contouring, and low-resolution visual documentation. These factors introduce potential georeferencing errors, which we estimate to be on the order of a few meters horizontally. Nevertheless, the relative positioning of major morphological features, such as the summit cone, remains robust and provides a meaningful reference for comparison with modern UAV-derived geomagnetic data. In fact, the location of the historical cone aligns with the present-day negative magnetic anomaly corridor, supporting the interpretation that persistent subsurface pathways correspond to long-lived structural features of the Salse di Regnano system. The integration of historical cartography with modern UAV surveys, facilitated by the DigMap MATLAB workflow, thus enhances both the qualitative and quantitative understanding of the site.

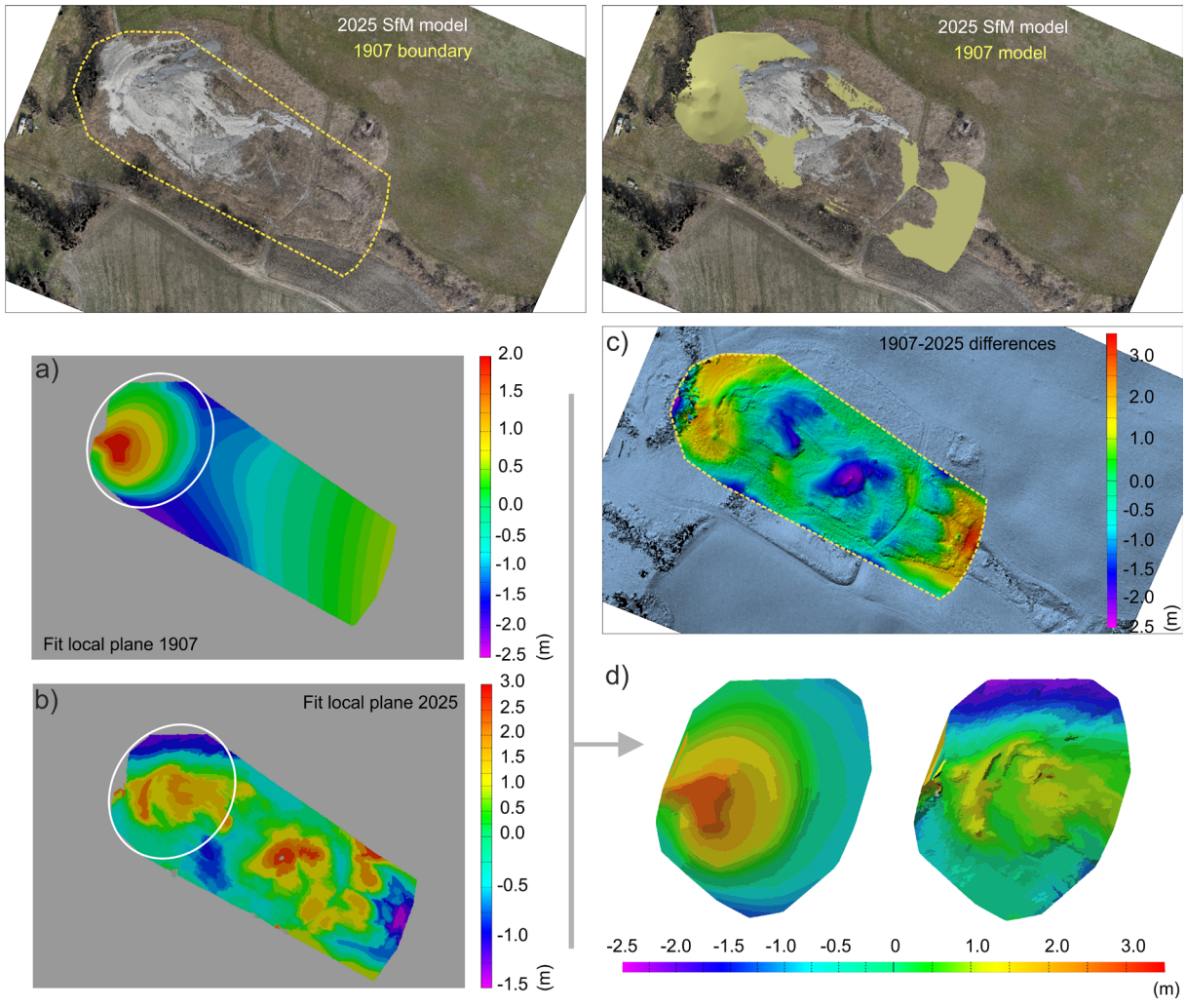

Figure 11. Comparison between the 1907 model and the current 2025 model. In the top panel, the SfM model with natural colors is shown, with the 1907 mud-volcano area outlined, and on the right the DEM superimposed to highlight morphological differences. (a) The 1907 model with a color scale emphasizing morphology, obtained as the distance between the model and the fitted reference plane of the area; (b) same as in (a) but using the 2025 model; (c) the 1907-2025 difference map, highlighting how the morphology evolved from past to present; (d) a detail of the summit sector where a conical structure was present, now disappeared following the 1930 paroxysmal event.

5. Conclusions

This study advances the understanding of the Salse di Regnano through a multidisciplinary approach integrating geological, geochemical, historical, and high-resolution UAV photogrammetric and geomagnetic data. The comparison between the 1907 reconstruction and present-day morphology reveals that the system has undergone substantial reorganization over the last century. Early mapping documents a markedly different landscape, dominated by a large conical edifice at the upper slope, which was subsequently reshaped, likely during the paroxysmal event around 1930, into the flatter, subdued morphology observed today. These changes are consistent with extensive ancient mud deposits documented in geological maps, confirming that the active zone currently visible is only a remnant expression of a once much larger and more dynamic system. Within this historical-geomorphological framework, the UAV-based geomagnetic survey adds a complementary view of the shallow subsurface. Distinct scalar magnetic anomalies cannot be explained by surface morphology alone. Forward modeling based on the DEM generates a synthetic magnetic field derived solely from topography. Comparison with the measured magnetic model indicates that morphology-induced fields could be weak, misaligned with the observed pattern, and only locally correlated. The characteristic north-south "tongue" of negative values extending toward the present active mud-emission area does not arise from topographic effects, while positive anomalies correspond to peripheral reliefs or minor morphostructural features. Local zones of high correlation or anticorrelation between the two models are mathematically expected wherever both fields exhibit regular shapes, and should not be interpreted as direct physical relationships. Interpreted within the broader PROMUD research framework, this comparison highlights persistent structural or lithological features that guide present-day mud emissions, contributing a piece to the overall mosaic of knowledge of the Salse di Regnano system. The low-value magnetic alignment acquires particular significance when interpreted in the context of historical and geological evidence. The corridor of negative anomalies crosses the modern active mud zone and aligns with the distribution of extensive, ancient mud-flow and mud-breccia deposits along the slope. This indicates that the current active vent likely follows a persistent subsurface pathway, with the magnetic signature marking a structurally or lithologically weakened sector, potentially still rich in fluids. Such an interpretation is consistent with studies of mud-volcano conduits and fluid ascent systems in comparable sites (Kadirov and Gadirov, 2014; Mazzini and Etiope, 2017). Comparisons with historical reconstructions further support this view: the main negative magnetic "tongue" broadly corresponds to long-standing emission areas, while positive anomalies partially coincide with former vent positions or more consolidated conduits. The minor downslope shift of the anomaly relative to the 1907 cone reflects the gradual redistribution of clay-rich materials inferred from volumetric differences between the 1907 and 2025 models. In favorable shallow-subsurface settings, diagenetic processes such as microbial sulfate reduction and organic-complexed iron mobilization may produce heterogeneous magnetic mineral assemblages (pyrite and, in specific conditions, magnetite), leading to variable magnetic susceptibility. The UAV survey captures these variations, with negative anomalies reflecting mud-dominated, low-susceptibility zones, and positive anomalies marking more competent or ferromagnetic-enriched bodies. Preliminary stability checks confirm the internal consistency of UAV measurements, providing a reliable estimate of noise and uncertainty.zZ

Overall, by integrating multi-temporal morphological data with geomagnetic, normalized, and 3D datasets, this study shows that the present-day Salse di Regnano morphology, especially the subdued geometry of the modern cones, cannot be understood without considering the major 20th-century paroxysm and the extensive ancient mud deposits still shaping subsurface pathways. The geomagnetic alignment of low values highlights a persistent corridor linking the upper slope deposits to the current active vent, revealing subsurface patterns not evident from topography alone.

Future work should include complementary geophysical methods, such as electrical resistivity tomography and passive seismic monitoring (Romano et al., 2023; Carfagna et al., 2024), to better resolve fluid conduits and dynamic processes. The progressive investigative framework presented here, building on Pesci et al. (2025b), will support semi-automated workflows for multi-temporal data integration, enabling systematic interpretation across scales and operational scenarios. In particular, the integration of geophysical measurements with high-resolution morphological data will provide specific, local constraints on subsurface structures, allowing the formulation of preliminary hypotheses on the depth and extent of fluid-bearing conduits. Furthermore, additional UAV magnetometry surveys, conducted across different time intervals and flight sessions, are planned to obtain dense, aligned profiles that can serve as robust constraints for inversion models. These inversion-based approaches, typically sensitive to measurement noise, are expected to be particularly reliable in this case due to the high internal stability and consistency of the collected magnetic data, enabling the generation of a magnetic tomographic model that extends

local depth estimates to a broader area. This combined approach supports ongoing updates to the conceptual model, contributing to a clearer understanding of the Salse di Regnano system and its evolving morphological and geophysical characteristics.

Data availability statement. Data are available from the authors upon request.

Acknowledgements. The authors gratefully acknowledge Paola Cusano for coordinating the Pianeta Dinamico PROMUD project, and Giancarlo Tamburello for his invaluable support during UAV survey operations.
We also thank our colleagues from the University of Bologna for assistance.

References

Accaino, F., A. Bratus, S. Conti, D. Fontana et al. (2007). Fluid seepage in mud volcanoes of the northern Apennines: An integrated geological and geophysical study, J. Appl. Geophys., 63, 90-101, doi:10.1016/j.jappgeo.2007.01.004.

Accomando, F., A. Bonfante, M. Buonanno, G. Florio et al. (2022). Mapping an igneous dike in carbonate rocks by drone-borne magnetometry. Paper presented at the NSG2022 3rd Conference on Airborne, Drone and Robotic Geophysics, 18-22 September 2022, Belgrade, Serbia, doi:10.3997/2214-4609.202220022.

Accomando, F. and G. Florio (2024). Drone-borne magnetic gradiometry in archaeological applications, Sensors, 24, 13, 4270, doi:10.3390/s24134270.

Accomando, F., A. Barone, F. Mercogliano, M. Milano et al. (2025). Advances in magnetic UAV sensing: A comparative study of the MagNimbus and MagArrow magnetometers, Sensors, 25, 19, 6076, doi:10.3390/s25196076.

Biasutti, R. (1907). Materiali per lo studio delle salse – Le salse dell'Appennino Settentrionale, Memorie Geografiche, 2, 101-255.

Blakely, R. J. (1995). Potential Theory in Gravity and Magnetic Applications, Cambridge University Press, Cambridge.

Bonaposta, D., M. T. De Nardo and S. Segadelli (2018). Historically documented activations of significant mud volcanoes near the Northern Apennine margin, In European Geosciences Union General Assembly 2018, 8-13 April 2018, Vienna, Austria.

Boschi, F. (2012). Magnetic prospecting for the archaeology of Classe (Ravenna), Archaeological Prospection, 19, 3, 219-227, doi:10.1002/arp.1430.

Bonini, M. (2009). Mud volcanoes: Indicators of stress orientation and tectonic controls, Earth-Sci. Rev., 97, 117-140, doi:10.1016/j.earscirev.2009.08.002.

Brighenti, F., F. D'Ajello Caracciolo, I. Nicolosi and F. Speranza (2020). Integrated geophysical investigation of shallow structures feeding mud volcanoes in the northern Apennines, J. Volcanol. Geotherm. Res., 401, 106964, doi:10.1016/j.jvolgeores.2020.106964.

Carfagna, N., A. Brindisi, E. Paolucci and D. Albarello (2024). Seismic monitoring of gas emissions at mud volcanoes: The case of Nirano (northern Italy), J. Volcanol. Geotherm. Res., 446, 107993, doi:10.1016/j.jvolgeores.2023.107993.

Caratori Tontini, F. (2012). 3-D focused inversion of near-seafloor magnetic data with application to the Brothers volcano hydrothermal system, Southern Pacific Ocean, New Zealand, J. Geophys. Res.: Solid Earth, 117, B10, B10102, doi:10.1029/2012JB009349.

Cella, F. and M. Fedi (2015). High-resolution geophysical 3D imaging for archaeology by magnetic and EM data: The case of the Iron Age settlement of Torre Galli, Southern Italy, Surv. Geophys., 36, 6, 831-850, doi:10.1007/s10712-015-9341-3.

Cunningham, M., C. Samson, A. Wood and I. Cook (2018). Aeromagnetic surveying with a rotary-wing unmanned aircraft system: A case study from a zinc deposit in Nash Creek, New Brunswick, Canada, Pure Appl. Geophys., 175, 3145-3158, doi:10.1007/s00024-018-1876-6.

Dainelli, G. (1907). Le salse dell'Appennino settentrionale, Memorie Geografiche, 1, Suppl. aRivista Geografica Italiana.

De Nardo, M. T. (2019). Le salse dell'Emilia-Romagna: cartografie a confronto. Regione Emilia-Romagna. https://ambiente.regione.emilia-romagna.it/it/geologia/geologia/acque/risorse-montagna/salse-e-cartografia-1.

Ghirotto, A. (2023). Potential fields data modeling: new frontiers in forward and inverse problems. PhD Thesis, University of Genova.

Hammack, R., G. Veloski, M. Schlagenhauf, R. Lowe et al. (2020). Using drone-mounted geophysical sensors to map legacy oil and gas infrastructure (URTeC 2876). Paper presented at the Unconventional Resources Technology Conference, 20-22 July 2020, Austin, Texas, USA, doi:10.15530/urtec-2020-2876.

James, M. R. and S. Robson (2012). Straightforward reconstruction of 3D surfaces and topography with a camera: Accuracy and geoscience application, J. Geophys. Res. Earth Surf., 117, F03017. doi:10.1029/2011JF002289.

Kadirov, F. A. and A. H. Gadirov (2014). Model of mud volcano conduits inferred from geophysical and geodetic data (Azerbaijan). Proceedings of the Azerbaijan National Academy of Sciences, Earth Sciences, 69, 4, 3-12.

Kangaziyan, M., B. Oskooi and L. Namaki (2012). Investigation of the topography effect on the shape and polarity of magnetic anomalies, Boll. Geofis. Teor. Appl., 56, 1, 43-54, doi:10.4430/bgta0135.

Leucci, G., N. Masini, E. Rizzo, L. Capozzoli et al. (2015). Integrated archaeogeophysical approach for the study of a medieval monastic settlement in Basilicata, Open Archaeol., 1, 236-246, doi:10.1515/opar-2015-0014.

Lin, Z., L. Chang, A. P. Roberts, D. Heslop et al. (2021). A novel authigenic magnetite source for sedimentary magnetization. Geology, 49, 360-365, doi:10.1130/G48069.1.

Liu, S., X. Li and L. Zhang (2018). Three-dimensional inversion of magnetic data in the presence of topography and remanent magnetization, Geophys. J. Int., 215, 1, 614-628, doi:10.1093/gji/ggy206.

Malehmir, A., L. Dynesius, K. Paulusson, A. Paulusson et al. (2017). The potential of rotary-wing UAV-based magnetic surveys for mineral exploration: A case study from central Sweden, The Leading Edge, 36, 552-557, doi:10.1190/tle36070552.1.

Mazzini, A. and G. Etiope (2017). Mud volcanism: An updated review, Earth-Sci. Rev., 168, 81-112, doi:10.1016/j.earscirev.2017.03.001.

Mu, Y., X. Zhang, W. Xie and Y. Zheng (2020). Automatic detection of near-surface targets for unmanned aerial vehicle (UAV) magnetic survey, Remote Sensing, 12, 452, doi:10.3390/rs12030452.

Nespoli, M., M. Antonellini, D. Albarello et al. (2023). Gravity data allow to image the shallow-medium subsurface below mud volcanoes, Geophys. Res. Lett., 50, 19, e2023GL103505, doi:10.1029/2023GL103505.

Nicolosi, I., F. D'Ajello Caracciolo, A. Pignatelli and M. Chiappini (2019). Imaging the Bracciano caldera system by aeromagnetic data inversion (Sabatini Volcanic District, Central Italy), J. Volcanol. Geotherm. Res., 388, 106680, doi:10.1016/j.jvolgeores.2019.106680.

Nikulin, A. and T. S. de Smet (2019). A UAV-based magnetic survey method to detect and identify orphaned oil and gas wells, The Leading Edge, 38, 447-452, doi:10.1190/tle38060447.1.

Oppo, D. (2009). Studio dei vulcani di fango per la definizione della migrazione dei fluidi profondi. PhD Thesis, Università di Bologna.

Parvar, K., A. Braun, D. Layton-Matthews and M. Burns (2017). UAV magnetometry for chromite exploration in the Samail ophiolite sequence, Oman, J. Unmanned Vehicle Sys., 6, 57-69, doi:10.1139/juvs-2017-0012.

Pesci, A. and D. Randazzo (in press). DigMap (MATLAB) – Digitalizzazione e correzione di scala per mappe topografiche storiche/DigMap (MATLAB) – Digitization and scale correction of historical topographic maps, Rapporti Tecnici INGV.

Pesci, A., S. Amoroso, G. Teza and L. Minarelli (2018). Characterization of soil deformation due to blast-induced liquefaction by UAV-based photogrammetry and terrestrial laser scanning. Int. J. Remote Sens., 39, 22, 8317-8336, doi:10.1080/01431161.2018.1484960.

Pesci, A., G. Tamburello, F. Loddo, G. Teza et al. (2025a). Multidisciplinary investigation of the Salse di Regnano mud volcanoes (Northern Italy) using remote sensing and historical data, Ann. Geophys., doi:10.4401/ag-9366.

Pesci. A., G. Tamburello, G. Teza et al. (2025b). Drone-Based Photogrammetry and Morphological Characterization of the Salse del Dragone Mud Volcanoes: Integrating Multidisciplinary Data for Future Exploration, Ann. Geophys., doi:10.4401/ag-9292.

Pisciotta, A., G. Vitale, S. Scudero et al. (2021). A lightweight prototype of a magnetometric system for unmanned aerial vehicles, Sensors, 21, 14, 4691, doi:10.3390/s21144691.

Roberts, A. P. (2015). Magnetic mineral diagenesis, Earth-Sci. Rev., 151, 1-47.

Romano, G., M. Antonellini, D. Patella, A. Siniscalchi et al. (2023). Fluid conduits and shallow-reservoir structure defined by geoelectrical tomography at the Nirano Salse (Italy), Nat. Hazards Earth Syst. Sci., 23, 8, 2719-2735, doi:10.5194/nhess-23-2719-2023.

Romero-Toribio, M. C., F. Martín-Hernández and J. Ledo (2025). High-resolution drone-based aeromagnetic survey at the Tajogaite Volcano (La Palma, Canary Islands): Insights into its early post-eruptive shallow structure, Remote Sensing, 17, 3153, doi:10.3390/rs17183153.

Stoll, J. and D. Moritz (2013). Unmanned aircraft systems for rapid near surface geophysical measurements. In Proceedings of the 75th EAGE Conference & Exhibition-Workshops, 10-13 June 2013, London, UK, cp-349-00062, doi:10.3997/2214-4609.20130747.

Teza, G., A. Pesci and A. Galgaro (2016). Comparison of terrestrial laser scanning and UAV photogrammetry for surveying natural terrains, Geomorphology, 254, 70-81, doi:10.1016/j.geomorph.2015.10.018.

Walter, C. A., A. Braun and G. Fotopoulos (2019). Impact of three-dimensional attitude variations of an unmanned aerial vehicle magnetometry system on magnetic data quality, Geophys. Prospect., 67, 2, 465-479, doi:10.1111/1365-2478.12745.

Walter, C., A. Braun and G. Fotopoulos (2021). Characterizing electromagnetic interference signals for unmanned aerial vehicle geophysical surveys, Geophys., 86, 6, J21-J32, doi:10.1190/geo2020-0895.1.

Westboy, M. J., J. Brasington, N. F. Glasser, M. J. Hambrey and J. M. Reynolds (2012). 'Structure-from-Motion' photogrammetry: A low-cost, effective tool for geoscience applications, Geomorph., 179, 300-314, doi:10.1016/j.geomorph.2012.08.021.

Yamazaki, Y. and A. Maute (2017). Sq and EEJ – A review on the daily variation of the geomagnetic field caused by ionospheric dynamo currents, Space Sci. Rev., 206, 1, 299-405, doi:10.1007/s11214-016-0282-z.

***CORRESPONDING AUTHOR: Arianna PESCI**,
Istituto Nazionale di Geofisica e Vulcanologia, Sezione di Bologna, Bologna, Italy
e-mail: arianna.pesci@ingv.it